Simultaneous shifts in pressure and electric field boost the caloric response in ferroelectrics - Supplementary Information

Ming Zeng<sup>1</sup>, Michela Romanini<sup>1</sup>, Ivana Gorican<sup>2,3</sup>, Silvo Drnovsek<sup>2</sup>, Hana Ursic<sup>2,3</sup>, Alejandro Salvatori<sup>1</sup>, María Barrio<sup>1</sup>, Sophie Loehle<sup>4</sup>, Nicolas Obrecht<sup>4</sup>, Carlos Escorihuela-Sayalero<sup>1</sup>, Claudio Cazorla<sup>1</sup>, Àlvar Torelló<sup>1\*</sup>, Pol Lloveras<sup>1\*</sup>, Josep-Lluís Tamarit<sup>1</sup>

<sup>1</sup>Group of Characterization of Materials, Department of Physics and Barcelona Research Center in Multiscale science and Engineering, Universitat Politècnica de Catalunya, Av. Eduard Maristany 10-14, 08019, Barcelona, Catalonia, Spain.

<sup>2</sup>Electronic Ceramics Department, Jozef Stefan Institute, Jamova Cesta 39, 1000 Ljubljana, Slovenia.

<sup>&</sup>lt;sup>3</sup>Jozef Stefan Postgraduate School, Jamova Cesta 39, 1000 Ljubljana, Slovenia.
<sup>4</sup>TotalEnergies OneTech, 69360, Solaize, 08019, France.

<sup>\*</sup>Corresponding author(s). E-mail(s): alvar.torello@upc.edu; pol.lloveras@upc.edu;

# 1 Field-dependent experimental setup for calorimetry and dielectric spectroscopy

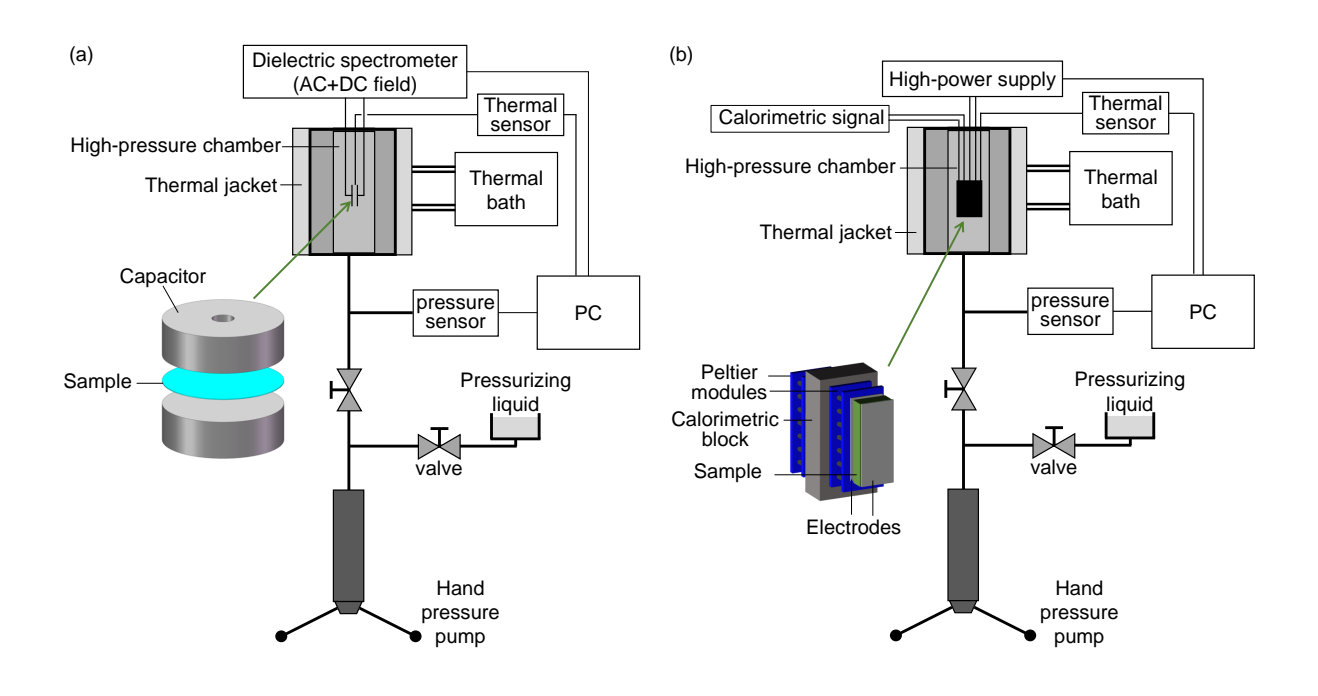


Fig. S1 Schematics of the experimental setups to perform (a) dielectric spectroscopy and (b) calorimetry under applied electric field and hydrostatic pressure.

### 2 Density Functional Theory results

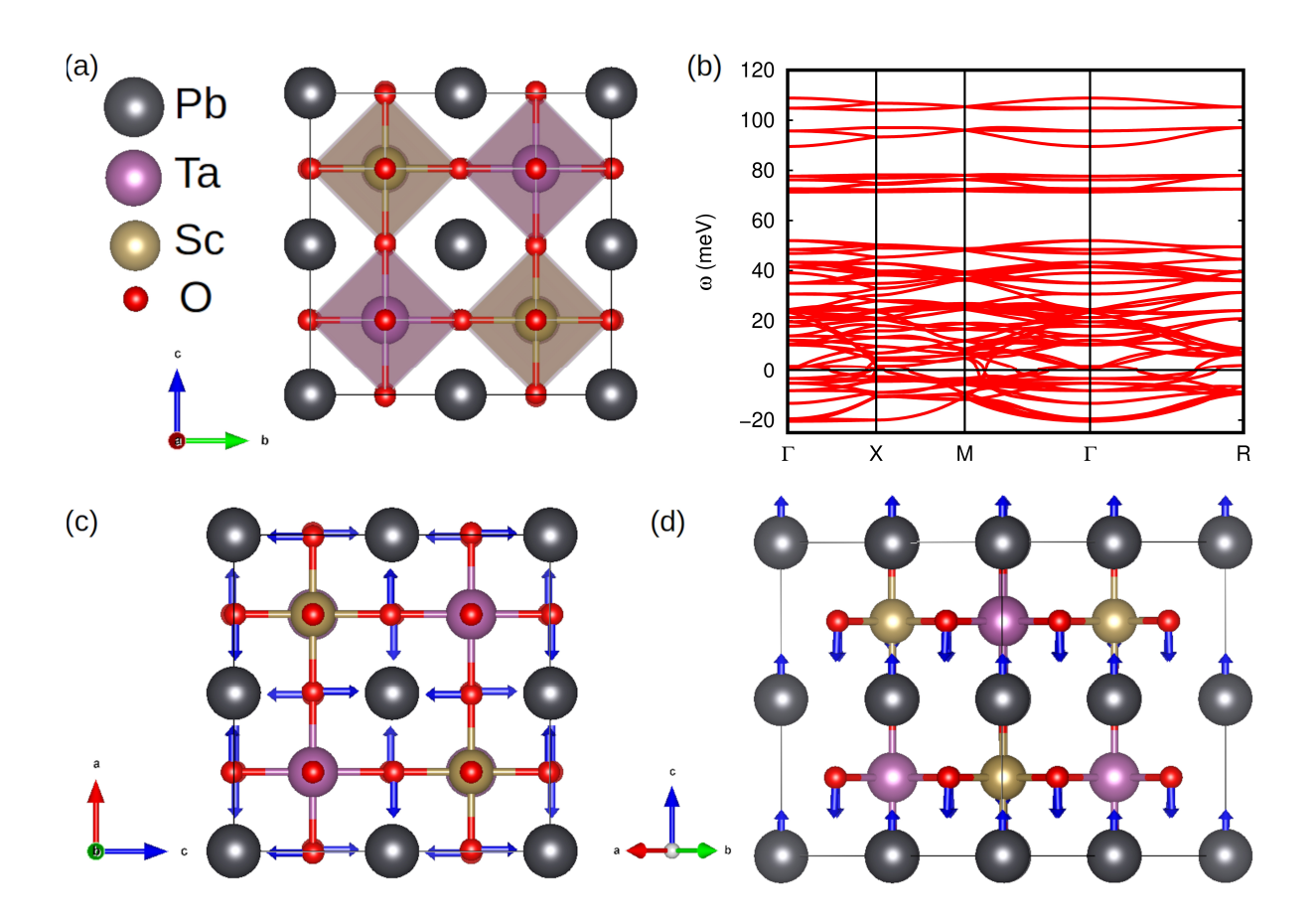


Fig. S2 Theoretical first-principles characterization of PST in the paraelectric cubic phase (space group  $Fm\bar{3}m$ ). (a) Sketch of the 40-atoms unit cell employed in the DFT simulations. (b) Computed phonon spectrum; imaginary phonon frequencies are represented with negative values. (c) Sketch of the atomic displacements (blue arrows) associated with the lowest-energy antiferrodistortive (i.e., oxygen octahedral rotations) vibrational instability estimated at  $\Gamma$ . (d) Sketch of the atomic displacements (blue arrows) associated with the lowest-energy polar vibrational instability estimated at  $\Gamma$ .

#### 3 Structural and microstructural analysis

The ceramic pellets were crushed, and X-ray diffraction (XRD) data were acquired with the PANalytical X'Pert PRO (Malvern Panalytical, Malvern, UK) using Cu-K $_{\alpha 1}$  radiation. The XRD pattern was measured in the  $2\theta$  range from  $10^{\circ}$  to  $70^{\circ}$  with a step of  $0.034^{\circ}$  and a dwell time of 100 s per step and is shown in Fig. S3(a). The (111) and (200) peaks from the XRD pattern were used to determine the degree of ordering  $\Omega$  by Eq. 4 from Ref. [1]:

$$\Omega^2 = \frac{\left(\frac{I_{111}}{I_{200}}\right)_{exp}}{\left(\frac{I_{111}}{I_{200}}\right)_{(theor,\Omega=1)}} \tag{1}$$

The  $\Omega$  was calculated to be 0.87, as described in the Results section of the article. For the theoretical ratio of peak intensities  $I_{111}/I_{200}$ , the value 1.33 was taken as suggested in Ref. [2].

The microstructure of the sintered ceramics was investigated using a field-emission scanning electron microscope (FE-SEM, JSM-7600 F, Jeol Ltd., Japan). Prior to microstructural analysis, the samples were fractured for fracture-surface examination, ground and polished with diamond paste and fine polished using OP-S colloidal silica suspension (Struers, Denmark) for polished-surface examination, and thermally etched at  $\sim 950^{\circ}$ C for etched-surface examination and grain size evaluation. The FE-SEM micrographs are shown in Fig. S3(b). The average grain size of  $(1.2\pm0.7)~\mu$ m was evaluated from the digitized images of the etched surfaces processed by Image Tool software (UTHSCSA Image Tool Version 3.00. 2002) by measuring more than 450 grains. The grain size is expressed as the Feret's diameter [3].

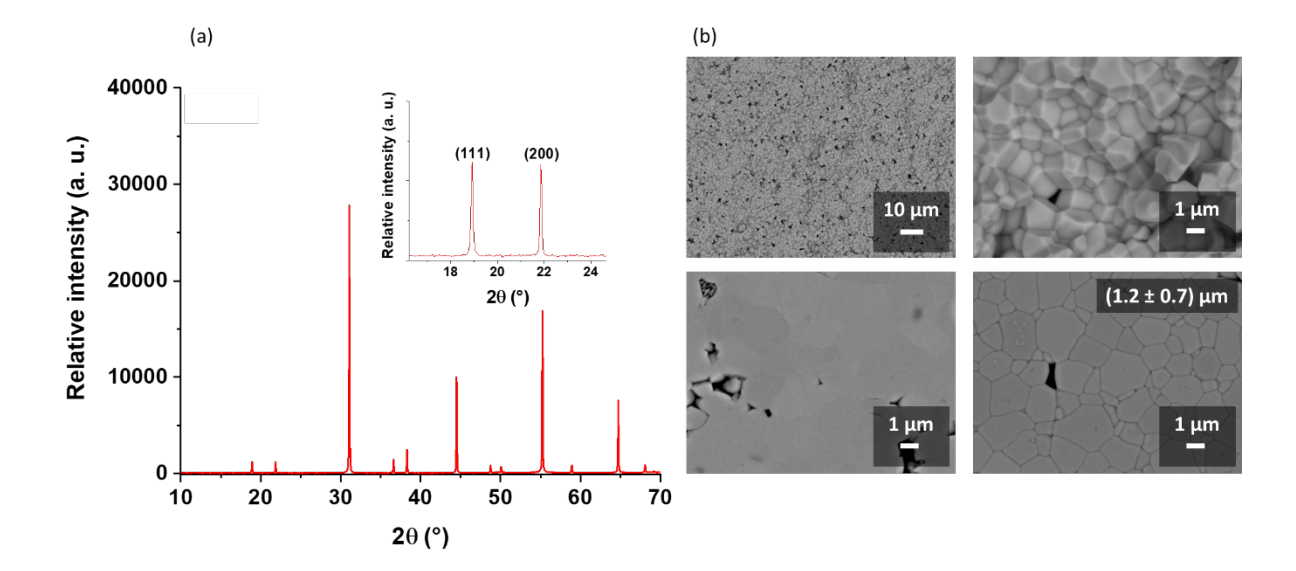


Fig. S3 (a) X-ray spectra of crushed PST ceramics. The inset shows the region measured in the  $2\theta$  range from  $17^{\circ}$  to  $24^{\circ}$ . (b) FE-SEM micrographs of the crushed (top left and right), polished (bottom left) and thermally etched (bottom right) surface of the PST ceramic.

#### 4 Calorimetry at atmospheric pressure

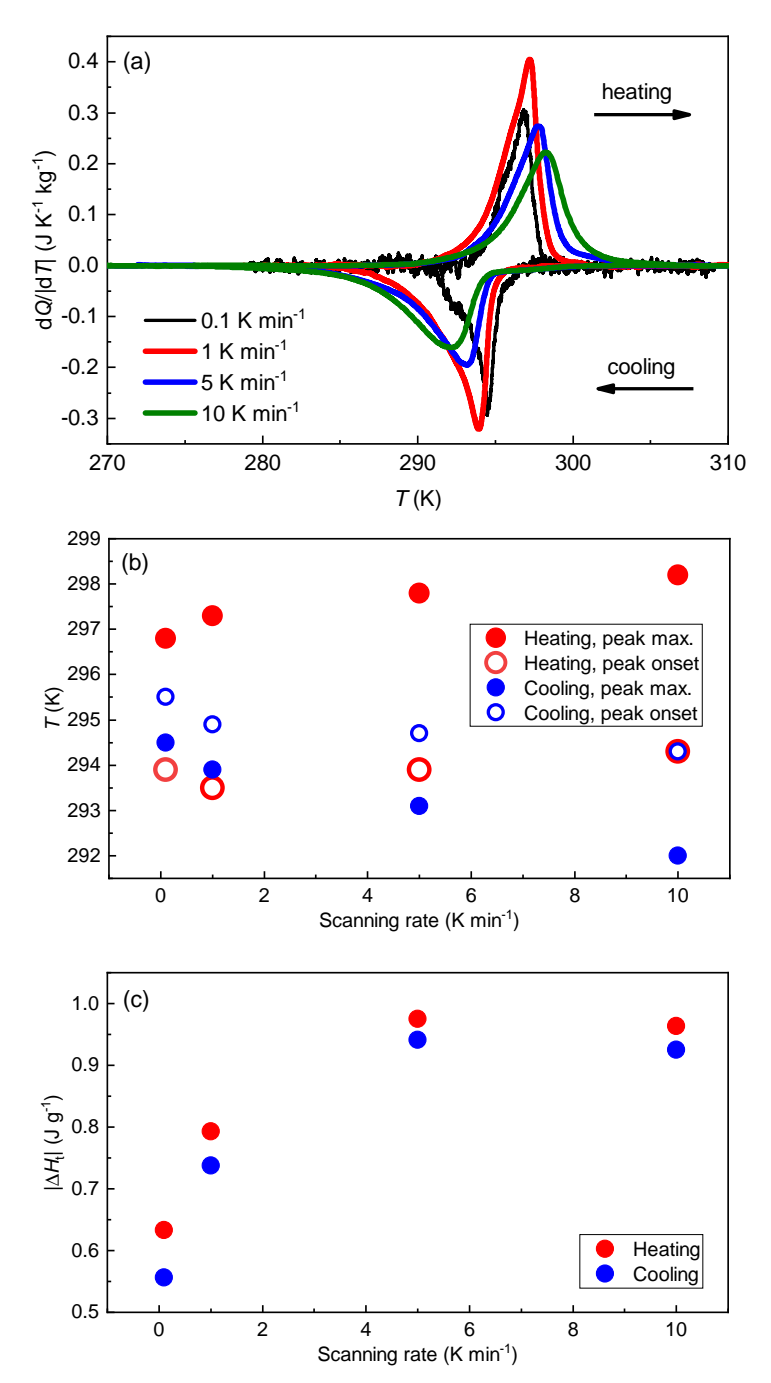


Fig. S4 Differential Scanning Calorimetry at atmospheric pressure for different scanning rates. (a) Thermograms. (b) Maximum (solid symbols) and onset (empty symbols) of the transition peak. (c) Transition enthalpy change obtained by integration of the DSC signals. In (b) and (c) red and blue symbols stand for heating and cooling runs, respectively.

## 5 Differential Thermal Analysis (DTA) under pressure and electric field

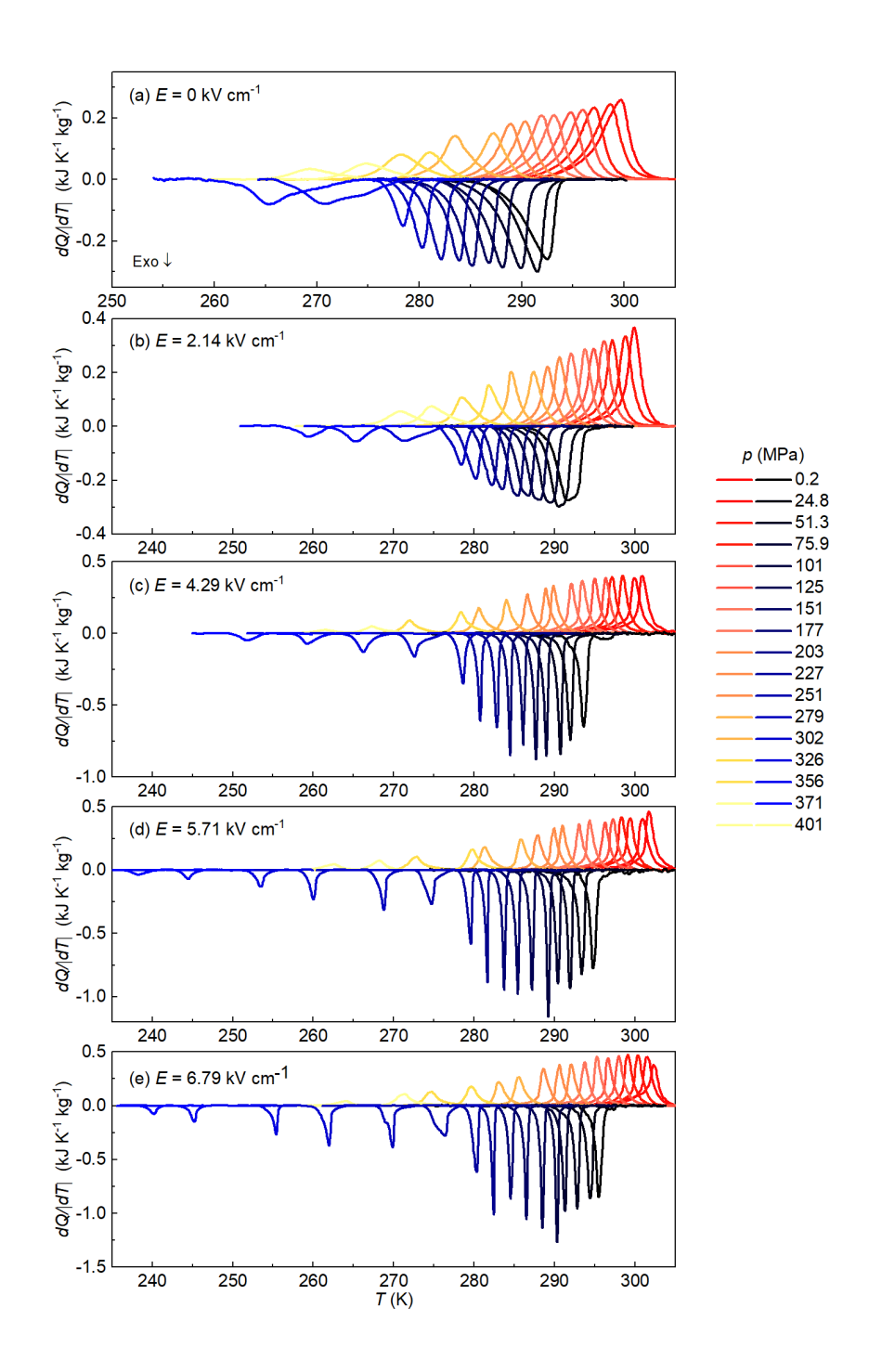


Fig. S5 Full set of measured DTA thermograms after baseline subtraction as a function of temperature for different values of applied pressure and electric field.

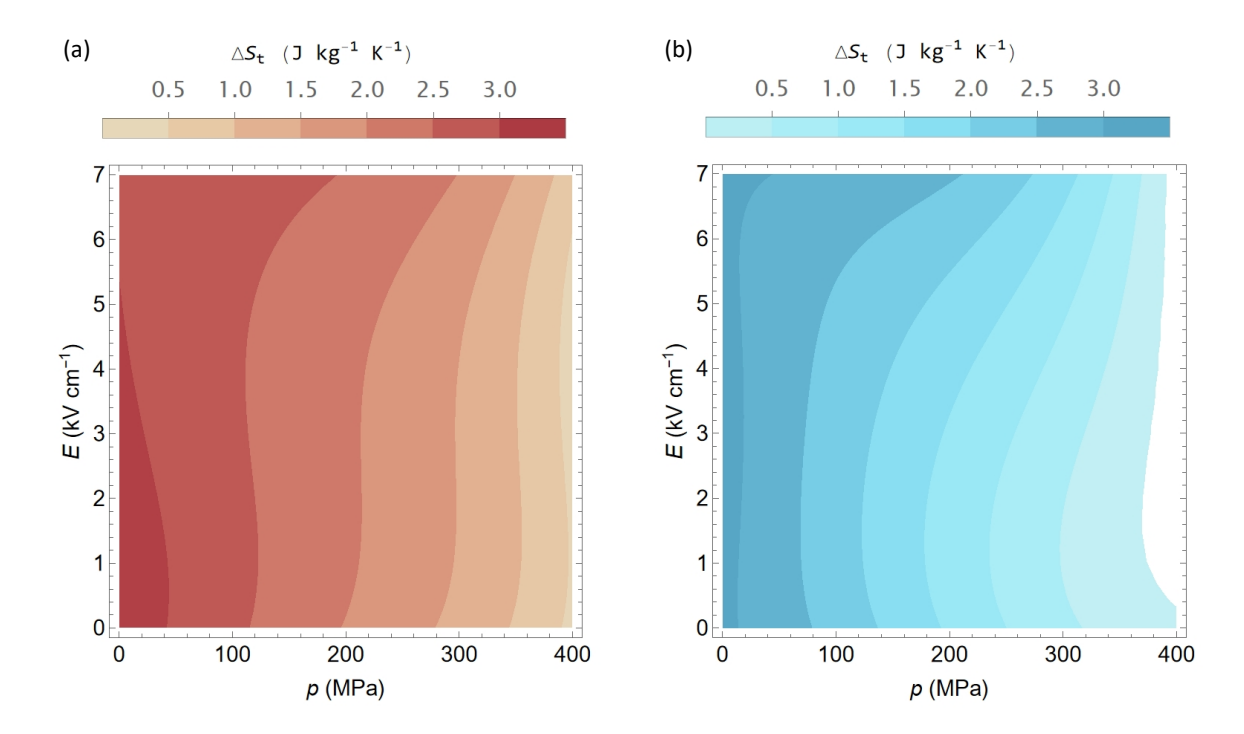


Fig. S6 Transition entropy change as a function of pressure and electric field, on heating (a) and on cooling (b) obtained by a smooth fitting of the values calculated via integration of DTA peaks after baseline subtraction.

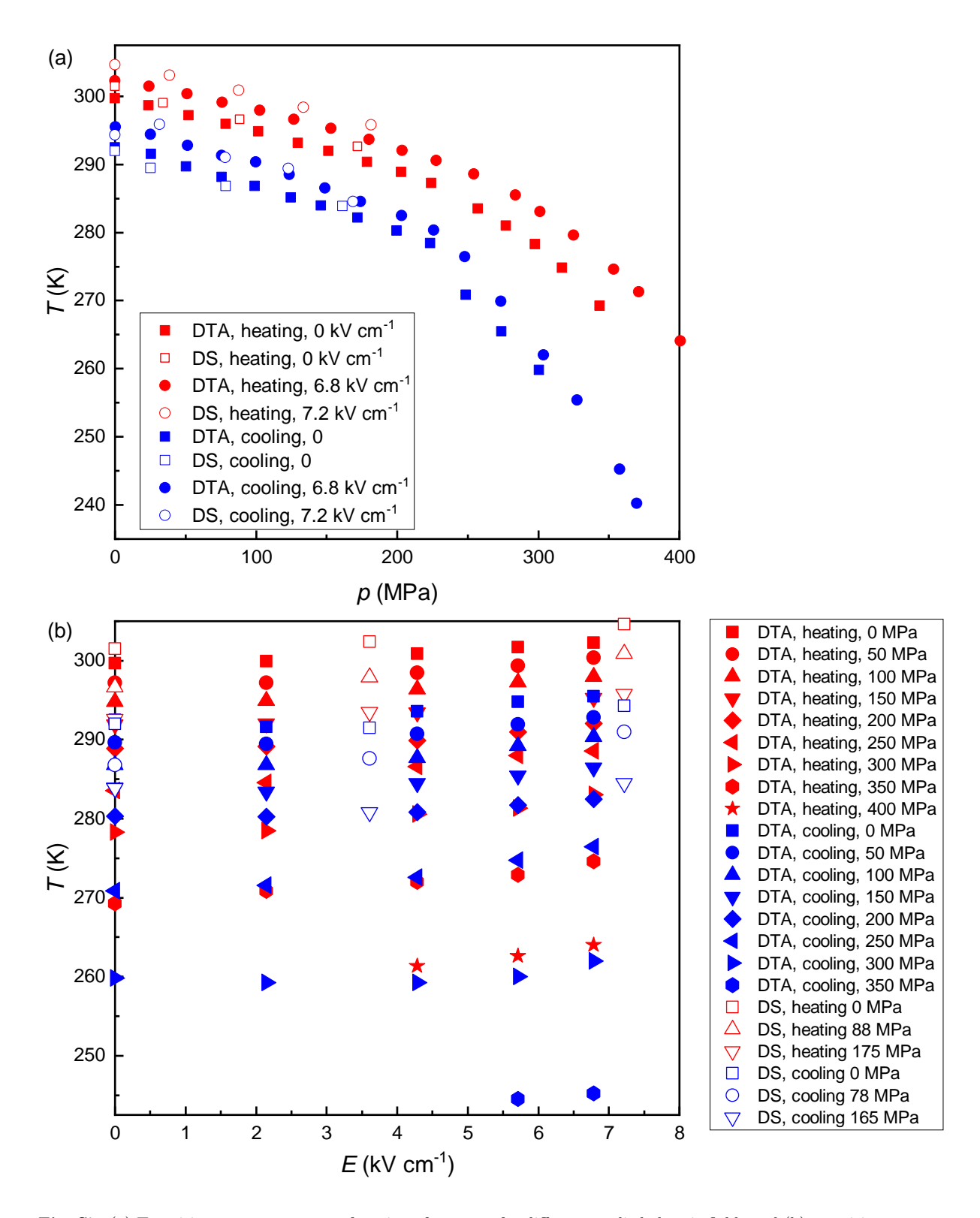


Fig. S7 (a) Transition temperature as a function of pressure for different applied electric fields and (b) transition temperature as a function of electric field for different applied pressure, as determined from DTA (solid symbols) and Dielectric Spectroscopy (DS, empty symbols). Discrepancies between the two sets of data are due to the imprecise determination of the transition temperature from the DS peaks.

## 6 Determination of the temperature-, pressure- and electric field-dependent entropy

The temperature-, pressure- and electric field-dependent entropy S(T, p, E) of a system undergoing a first-order phase transition can be expressed with respect to a reference entropy  $S(T_0, p_{\text{atm}}, 0)$  as

$$S(T, p, E) = S(T_0, p_{\text{atm}}, 0) + \int_0^T \frac{1}{T'} \left( C_p + \frac{dQ}{dT'} \right) dT' - \int_{p_{\text{atm}}}^p \left( \frac{\partial V}{\partial T} \right)_{p', E} dp' + \int_0^E \left( \frac{\partial P}{\rho \partial T} \right)_{p, E'} dE' \quad (2)$$

Here  $\frac{dQ}{dT}$  is the measured p- and E-dependent heat flow after baseline subtraction accounting for the entropy change at the transition and  $C_p$  is the heat capacity at constant fields p and E. The last two terms at the right side of the last equation are derived from Maxwell relations and represent isothermal entropy changes in individual phases outside the transition driven by pressure,  $\Delta S_+(p_{\rm atm} \to p)$ , and electric field,  $\Delta S_+(0 \to E)$  (where  $\rho$  is density). Calculation details are given in the following sections.

### 6.1 Construction of the temperature-, pressure- and electric field-dependent heat capacity

Heat capacity  $C_p$  at constant p and E was constructed as  $C_p = xC_p^{\rm I} + (1-x)C_p^{\rm II}$ . Here x(T,p,E) is the system fraction in the high-temperature phase determined from cumulative integration from DTA peaks using the following expression:

$$x(T, p, E) = \frac{\int_{T_1(p, E)}^{T} \frac{dQ(T, p, E)}{T'dT'} dT'}{\int_{T_1(p, E)}^{T_2(p, E)} \frac{dQ(T, p, E)}{TdT} dT}$$
(3)

where  $T_1(p, E)$  and  $T_2(p, E)$  are temperatures conveniently chosen before and after the transition for integration of DTA peaks after baseline subtraction. In turn,  $C_p^{\rm I}$  and  $C_p^{\rm II}$  are the heat capacities of the paraelectric and ferroelectric phases at atmospheric pressure and without any applied electric field, and are taken from literature [4]. Moreover,  $C_p^{\rm I}$  and  $C_p^{\rm II}$  were assumed to be independent of p and E within the field ranges under study. Their values were extrapolated to the temperature interval required by the field-driven transition shift as given by DTA measurements. The constructed temperature-, pressure- and electric field-dependent heat capacity functions  $C_p$  used in Eq. 2 for the determination of the entropy functions are shown in Fig. S8.

#### 6.2 Additional effects in individual phases

In this section we analyze isothermal entropy changes in individual phases outside the transition driven by pressure,  $\Delta S_+(p_{\rm atm} \to p)$ , and electric field,  $\Delta S_+(0 \to E)$ . According to literature data [5–7], both phases show small thermal expansion. Assuming this term to be independent of pressure, we estimate  $\Delta S_+(p_{\rm atm} \to p) \leq 0.5 \text{ J K}^{-1} \text{ kg}^{-1}$  upon pressure changes of  $\sim 200 \text{ MPa}$ . Therefore, we neglect this term in the low-temperature phase, which is consistent within uncertainty with very small values for  $\Delta S_+(p_{\rm atm} \to p)$  obtained in the high-temperature phase.

As for  $\Delta S_+(0 \to E)$ , we also assume  $\left(\frac{\partial P}{\rho \partial T}\right)_E$  to be independent of the electric field, which should result in an upper threshold for this contribution. Using literature data [1], we estimate  $\Delta S_+(0 \to E) \sim 0.15 \text{ J K}^{-1} \text{ kg}^{-1}$  for the low-temperature phase and  $\Delta S_+(0 \to E) \sim 0$  for the high-temperature phase upon electric field changes of  $\Delta E \sim 6 \text{ kV cm}^{-1}$ . Therefore, this term is also neglected in the construction of the entropy functions.

Considering the uncertainties associated with the aforementioned approximations and those arising due to the background to noise ratio in field-dependent calorimetry, we estimate an uncertainty of about 20% in the maximum values obtained for the caloric effects under maximum field changes.

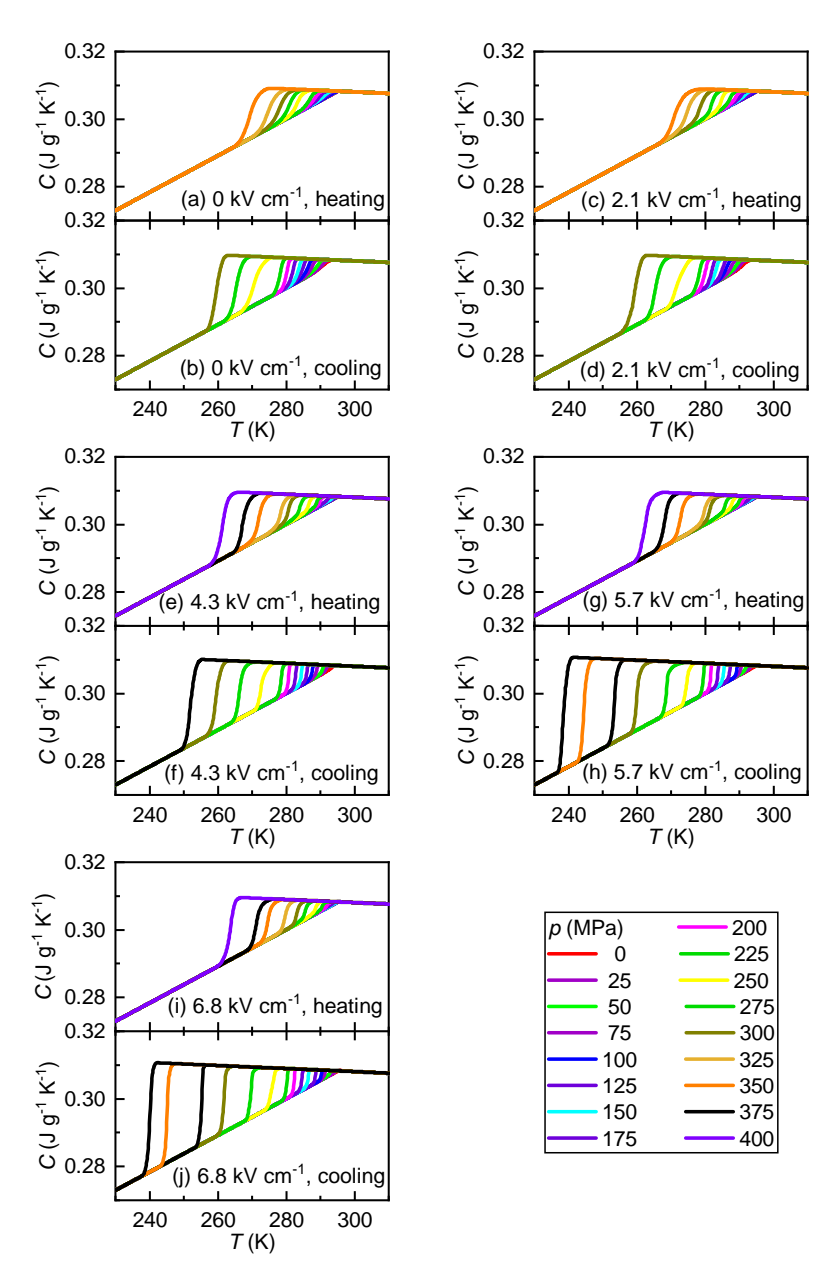


Fig. S8 Temperature-, pressure- and electric field-dependence heat capacity. For the calculation details see the text.

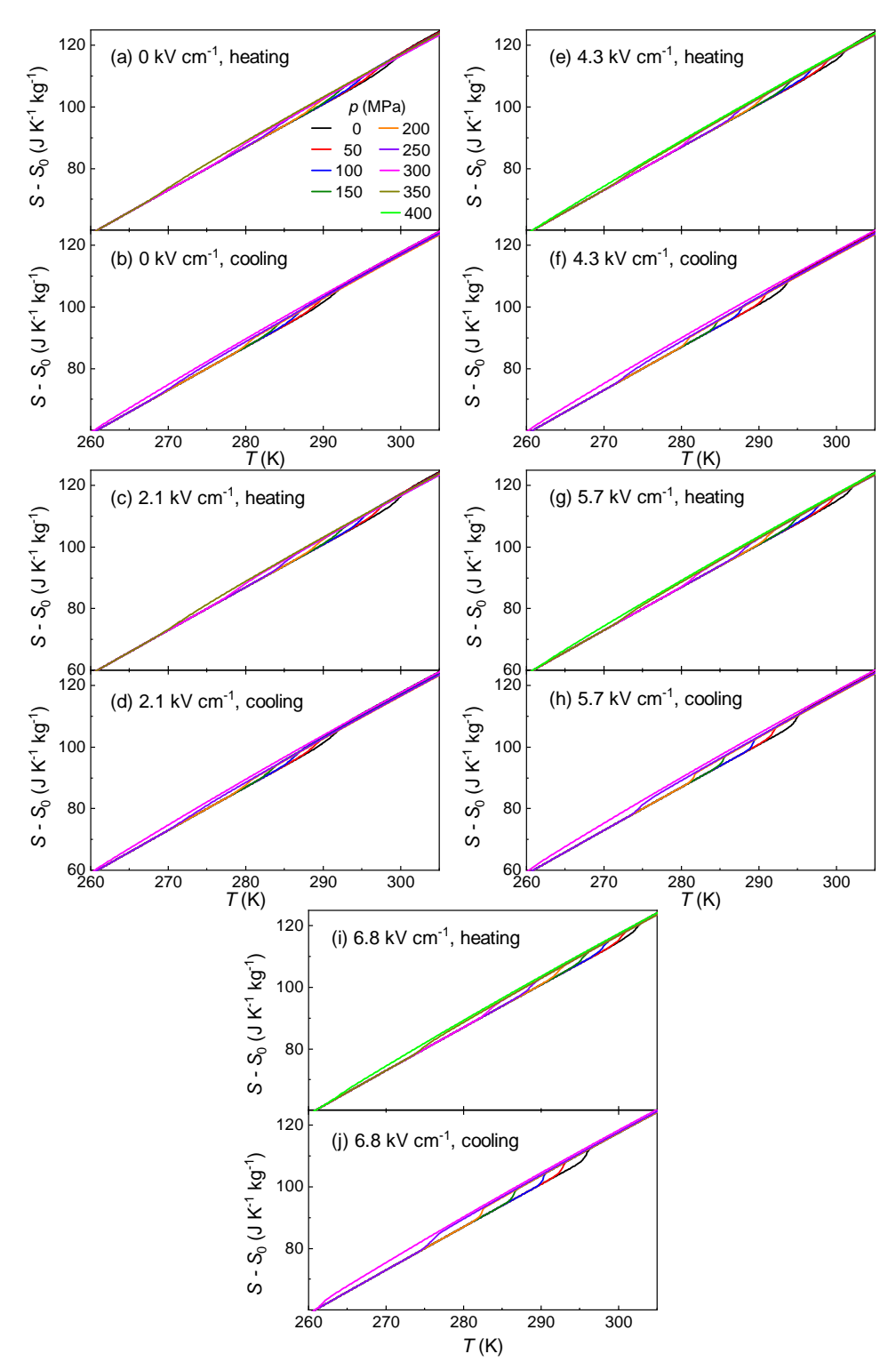


Fig. S9 Isofield entropy as a function of temperature for different values of pressure and electric field. Legend in panel (a) applies for all panels.

## 7 Thermodynamics of multicaloric effects in a pV - EP - T system

The thermodynamics of multicaloric effects that are relevant to ferroelectric compounds involves the generalized coordinates volume V and polarization P, and the corresponding conjugate fields pressure p and electric field E. Given the state function entropy S(T, p, E) (T is temperature), isothermal entropy changes  $\Delta S$  occurring due to changes in p ( $p_0 \to p_1$ ) and E ( $E_0 \to E_1$ ) can be expressed as a sequence of two monocaloric processes, i.e. each associated with the change in only one field. For instance, considering a sequence of changing first p and then E:

$$\Delta S(T, p_0 \to p_1, E_0 \to E_1) = \Delta S(T, p_0 \to p_1, E_0) + \Delta S(T, p_1, E_0 \to E_1) \tag{4}$$

where  $\Delta S(T, p_0 \to p_1, E_0)$  is the BC effect taking place at constant  $E_0$  and  $\Delta S(T, p_1, E_0 \to E_1)$  is the EC effect taking place at constant  $p_1$ . It is straightforward to see that this last term can be decomposed in the following sequence of paths:

$$\Delta S(T, p_1, E_0 \to E_1) = \Delta S(T, p_1 \to p_0, E_0) + \Delta S(T, p_0, E_0 \to E_1) + \Delta S(T, p_0 \to p_1, E_1)$$
 (5)

Inserting Eq. 5 in Eq. 4 we obtain:

$$\Delta S(T, p_0 \to p_1, E_0 \to E_1) = \Delta S(T, p_0 \to p_1, E_0)$$
 (6)

$$+\Delta S(T, p_0, E_0 \to E_1) + \Delta S(T, p_0 \to p_1, E_1) + \Delta S(T, p_1 \to p_0, E_0)$$
 (7)

$$= \Delta S(T, p_0 \to p_1, E_0) + \Delta S(T, p_0, E_0 \to E_1) + \Delta S_{cc}$$
 (8)

where in Eq. 8 we have identified the cross-coupling contribution  $\Delta S_{\rm cc}$  as the difference between the multicaloric effects obtained when changing both p and E and the summation of the monocaloric effects when changing only  $p_0 \to p_1$  (at  $E_0$ ) and only  $E_0 \to E_1$  at (at  $p_0$ ). Using the integral form  $\Delta S(T, p_0 \to p_1) = \int_{p_0}^{p_1} \left(\frac{\partial S}{\partial p}\right)_T dp$  from the exact differential property for S at constant T, we can express:

$$\Delta S_{\rm cc} = \Delta S(T, p_0 \to p_1, E_1) + \Delta S(T, p_1 \to p_0, E_0)$$

$$\tag{9}$$

$$= \int_{p_0}^{p_1} \left(\frac{\partial S}{\partial p}\right)_{T,E_1} dp - \int_{p_0}^{p_1} \left(\frac{\partial S}{\partial p}\right)_{T,E_0} dp \tag{10}$$

$$= \int_{p_0}^{p_1} \frac{\partial}{\partial p} \left[ S(T, p, E_1) - S(T, p, E_0) \right]_T dp \tag{11}$$

$$= \int_{p_0}^{p_1} \frac{\partial}{\partial p} \left[ \Delta S(T, p, E_0 \to E_1) \right]_T dp \tag{12}$$

$$= \int_{p_0}^{p_1} \frac{\partial}{\partial p} \left[ \int_{E_0}^{E_1} \left( \frac{\partial P}{\rho \partial T} \right)_{p,E} dE \right]_T dp \tag{13}$$

$$= \int_{p_0}^{p_1} \int_{E_0}^{E_1} \frac{\partial}{\partial T} \left( \frac{\partial P}{\rho \partial p} \right)_{TE} dp dE \tag{14}$$

$$= \int_{p_0}^{p_1} \int_{E_0}^{E_1} \frac{\partial \chi_{12}(T, p, E)}{\partial T} dp dE$$
 (15)

where in Eq. 13 the Maxwell relation  $\Delta S(T, p_0, E_0 \to E_1) = \int_{E_0}^{E_1} \left(\frac{\partial P}{\rho \partial T}\right)_{p,E} dE$  has been used and in eq. 15 we have introduced the off-diagonal component of the cross-susceptibility tensor  $\chi_{12} \equiv \left(\frac{\partial P}{\rho \partial p}\right)_{T,E}$ . By exchanging E and p and using the Maxwell relation  $\Delta S(T, p_0 \to p_1, E_0) = -\int_{p_0}^{p_1} \left(\frac{\partial V}{\partial T}\right)_{p,E_0} dp$ , we then obtain that the cross-susceptibility tensor is symmetric,  $\chi_{12} = \chi_{21} \equiv \chi$ :

$$\chi \equiv \left(\frac{\partial P}{\rho \partial p}\right)_{T,E} = -\left(\frac{\partial V}{\partial E}\right)_{T,p} \tag{16}$$

These equations show that for materials with strong cross-response between generalized coordinates and non-conjugated fields, the multicaloric effects may be enhanced with respect to the monocaloric counterparts.

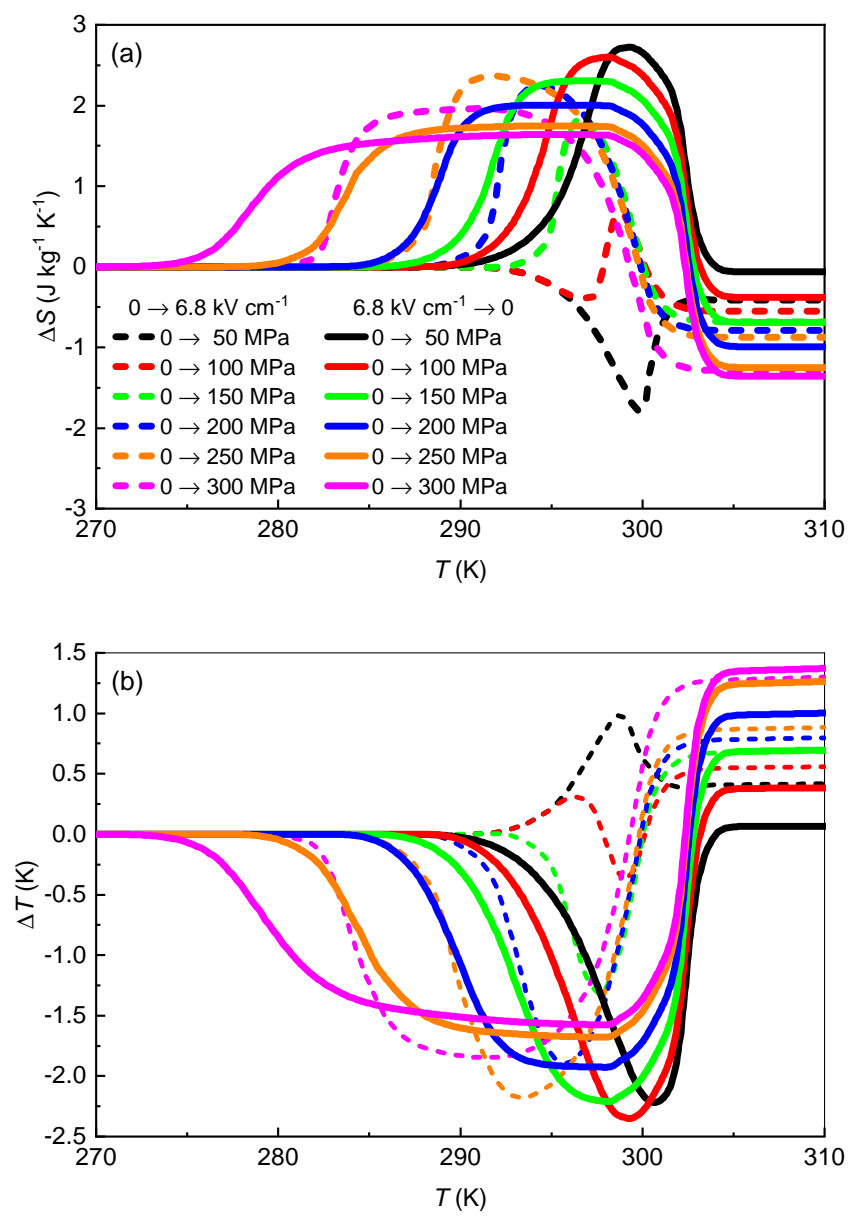


Fig. S10 (a) Isothermal entropy changes and (b) adiabatic temperature changes obtained on first application of electric field and pressure (in-phase, dashed lines) and on first application of electric field and removal of pressure (antiphase, solid lines). The optimized multicaloric response due to antiphase field changes compared to in-phase field changes can be observed.

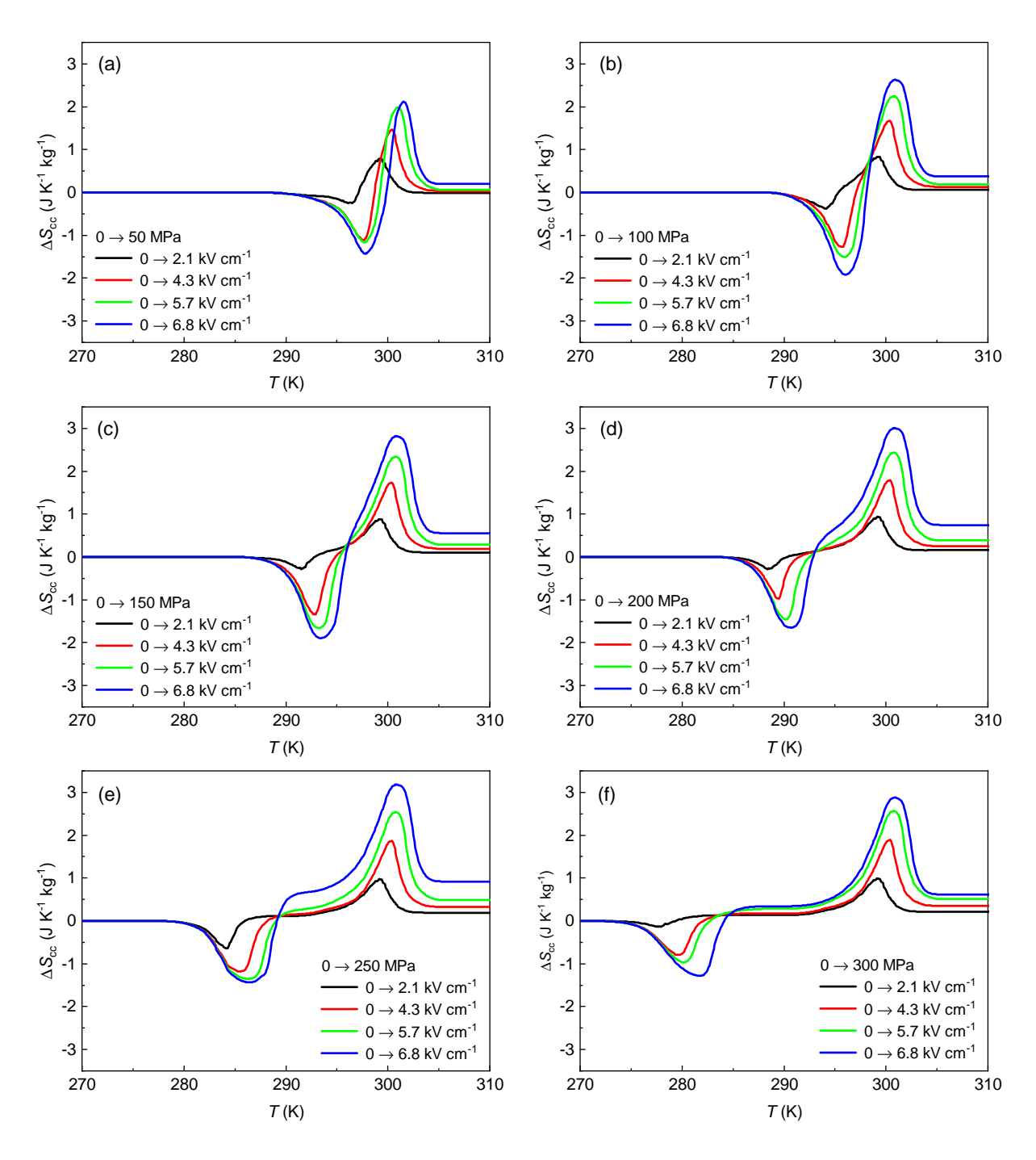


Fig. S11 Cross-coupling contribution  $\Delta S_{\rm cc}$  to the total isothermal entropy changes as a function of temperature for different values of pressure and electric field changes.

#### References

- [1] Shebanov, L., Birks, E., Borman, K.: X-ray studies of electrocaloric lead-scandium tantalate ordered solid solutions. Ferroelectrics **90**(1), 165–172 (1989)
- [2] Stenger, C.G., Burggraaf, A.: Order-disorder reactions in the ferroelectric perovskites  $Pb(Sc_{1/2}Nb_{1/2})O_3$  and  $Pb(Sc_{1/2}Ta_{1/2})O_3$  I. Kinetics of the ordering process. Phys. Status Solidi (a)  $\bf{61}(1)$  (1980)
- [3] Walton, W.: Feret's statistical diameter as a measure of particle size. Nature **162**(4113), 329–330 (1948)
- [4] Nair, B.: Electrocaloric applications based on multilayer capacitors of PbSc<sub>0.5</sub>Ta<sub>0.50</sub>O<sub>3</sub>. PhD thesis, University of Cambridge (2020)
- [5] Dul'kin, E., Salje, E.K., Aktas, O., Whatmore, R.W., Roth, M.: Ferroelectric precursor behavior of highly cation-ordered PbSc<sub>0.5</sub>Ta<sub>0.5</sub>O<sub>3</sub> detected by acoustic emission: tweed and polar nanoregions. Appl. Phys. Lett. 105(21) (2014)
- [6] Abdulvakhidov, K., Mardasova, I., Myasnikova, T., Vitchenko, M., Oshaeva, E.: Phase transitions in PbSc<sub>0.5</sub>Ta<sub>0.5</sub>O<sub>3</sub>. Tech. Phys. 55, 514–516 (2010)
- [7] Stern-Taulats, E., Lloveras, P., Barrio, M., Tamarit, J.-L., Planes, A., Mañosa, L., Whatmore, R., Mathur, N., Moya, X.: Asymmetric electrocaloric effects in PbSc<sub>0.5</sub>Ta<sub>0.5</sub>O<sub>3</sub> on field application and removal. arXiv preprint arXiv:2010.15705 (2020)